

See discussions, stats, and author profiles for this publication at: <https://www.researchgate.net/publication/240721327>

Experimental Evaluation of Interactive Buckle Localization in Compression Sandwich Panels

Article in *Journal of Sandwich Structures and Materials* · July 1999

DOI: 10.1177/109963629900100304

CITATIONS

17

READS

1,616

1 author:



[Ahmer Wadee](#)

Imperial College London

155 PUBLICATIONS 2,539 CITATIONS

[SEE PROFILE](#)

Some of the authors of this publication are also working on these related projects:



Nonlinear behaviour of under-deck cable stayed bridges [View project](#)



Nonlinear mechanics of lattice materials [View project](#)

Experimental Evaluation of Interactive Buckle Localization in Compression Sandwich Panels

M. Ahmer Wadee

Department of Mechanical Engineering, University of Bath,
Claverton Down, Bath, BA2 7AY *

Abstract

Experimental observations on the axially-loaded sandwich panel compare well with the recent developments in the theoretical modelling of interactive localized buckling. Comparisons of experimental collapse loads, buckle wavelengths and equilibrium paths with the theoretical model show good correlation.

Keywords: Experiments; Nonlinear buckling; Mode interaction;
Localization; Numerical continuation

1 Introduction

Recent work on the theory of interactive buckling in compression sandwich panels has shown that an initial buckle profile, usually an overall Euler-type buckling mode, is subsequently destabilized by a periodic local buckling mode after a secondary bifurcation. This nonlinear mode interaction tends to be a route to highly unstable localized buckling on one panel face plate [1, 2], and is thus very sensitive to initial imperfections [3]. This paper reports on physical experiments that have been carried out to validate the theoretical models. The experiments provide insight into the real behaviour exhibited by the panels; the transformation from pure compression to overall buckling to localization and plastic collapse is consistently observed. Although the theoretical model does not account explicitly for plasticity, in the absence of load reversal, the elastic range should provide enough information during loading to compare critical loads, wavelengths of localized buckling and load–end-shortening equilibrium paths with the models developed earlier.

2 Interactive Buckling Model

Structural sandwich panels, represented in Figure 1, are used in applications where weight efficiency has to be combined with high strength [4]. However, owing to the fact that they are efficient carriers of load in compression, they tend to exhibit nonlinear mode interaction effects [5, 6] involving an overall mode of buckling combined with a local mode of buckling [7, 8] introducing highly unstable localized buckling to one face [1].

*Published in *Journal of Sandwich Structures and Materials*, volume 1, issue 3, pages 230–254, 1999.

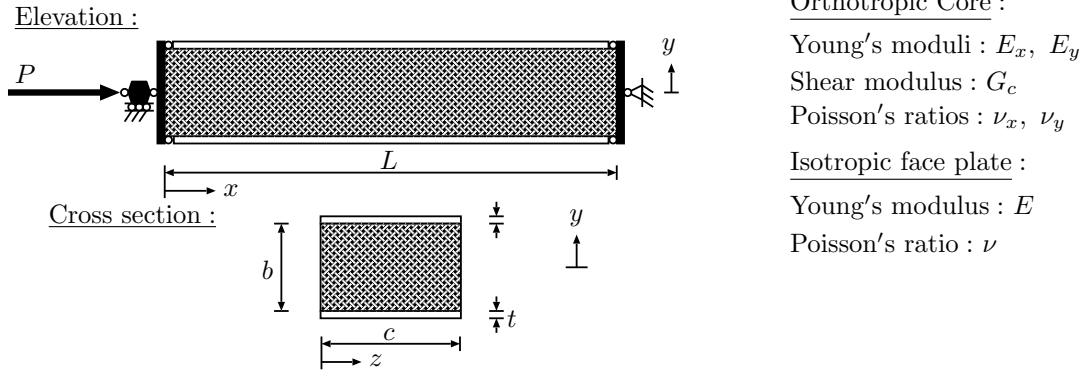


Figure 1: Sandwich panel loading configuration, cross-section and material properties.

In this section, the linear critical load formulation for each of the distinct buckling modes is summarized, followed by an abridged presentation of the formulation of the model to describe the sandwich panel's post-buckling behaviour. This lays the foundation for the numerical comparisons with the physical experiments.

2.1 Critical Buckling Loads

Periodic Rayleigh–Ritz analysis [9, 10, 11] was used to determine the important critical loads for the sandwich panel. For overall buckling, the core cannot be modelled by a Winkler-type foundation as this would implicitly assume the Euler–Bernoulli approximation that plane sections remain plane, denying shearing strains; this makes the face plates independent, and stops the possibility of local buckling. Thus, the effect of shearing in the core is accounted for by decomposing the overall half sine wave mode into separate *sway* and *tilt* components (Figure 2). For the local mode, a linear combination of *snake* (anti-symmetric) and *hourglass* (symmetric) modes with an associated wave number $i\pi x/L$ is employed such that one face remains unbuckled whilst the other face buckles periodically. Sway and tilt overall mode components W and θ with respective amplitudes q_s and q_t are:

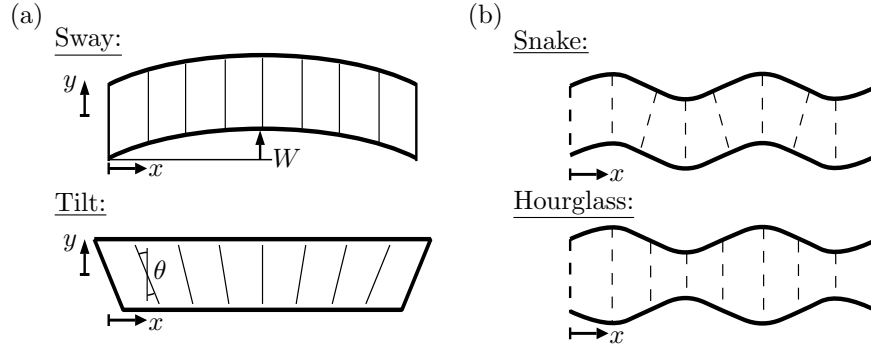


Figure 2: Decomposed modes for critical buckling: (a) Sway and tilt components of overall mode; (b) Snake and hourglass modes of local buckling.

$$W(x) = q_s L \sin \frac{\pi x}{L}, \quad \theta(x) = q_t \pi \cos \frac{\pi x}{L}. \quad (1)$$

Snake (N) and hourglass (H) modes for local buckling are:

$$W_N(x) = a_1 L \sin \frac{i\pi x}{L}, \quad \theta_N(x) = a_2 \pi \cos \frac{i\pi x}{L}, \quad W_H(x) = a_3 L \sin \frac{i\pi x}{L}. \quad (2)$$

Note that when one face remains straight, and the other face buckles periodically, $a_1 = a_3$.

Formulating the total potential energy, by summing contributions of strain energy of the faces in bending and axial compression (bending and membrane energy), the core in axial compression and shear (core energy) minus the work done by the load [2, 3], and applying linear eigenvalue analysis yields the respective critical loads for P [11]:

$$P_o^C = \frac{2\pi^2 EI}{L^2} + \frac{2Gb^2\pi^2}{L^2} \left[\frac{(D + \frac{C_x}{6})}{2G + \frac{b^2\pi^2}{L^2}(D + \frac{C_x}{6})} \right], \quad (3)$$

$$P_l^C = K \left[\frac{2\pi^2 EI i^2}{L^2} + \frac{kL^2}{\pi^2 i^2} + \frac{4G}{3} - \frac{2G^2}{\frac{\pi^2 i^2 b^2}{L^2}(D + \frac{C_x}{6}) + 2G} \right], \quad (4)$$

where P_o^C and P_l^C are the overall and local buckling loads respectively, and:

$$EI = \frac{Ect^3}{12(1 - \nu^2)}, \quad K = \frac{6Et(1 - \nu_x\nu_y) + 3E_cb}{6Et(1 - \nu_x\nu_y) + 2E_cb}, \quad D = \frac{Etc}{2}, \quad G = \frac{G_c cb}{2} \quad (5)$$

$$k = \frac{E_y c}{2(1 - \nu_x\nu_y)b}, \quad C_x = \frac{E_x bc}{2(1 - \nu_x\nu_y)}. \quad (6)$$

2.2 Nonlinear Buckling

The linear critical buckling analysis gives no indication of the true behaviour of the panel after buckling. Recent work has highlighted that interactive post-buckling responses can be triggered in compression sandwich panels. Moreover, these responses can tend to exhibit localization in practice which occur in severely unstable structures. A model formulated from variational principles has been developed [1, 2] that accounts for buckle localization from nonlinear modal coupling in sandwich panels. The interaction between overall and local buckling modes lead to a secondary bifurcation on *one* face plate when the overall mode introduces an extra bending moment at midspan as well as the axial-load, similar to a varying body force acting on the face plates [1]. This varying body force exceeds the local buckling load at midspan. The unstable nature of the post-buckling response is shown in Fig. 3, with the secondary bifurcation effectively reducing the load-carrying capacity of the panel.

The model requires two functions, $w(x)$ and $u(x)$, to describe, respectively, lateral and in-plane deflections of the face that localizes (Figure 4). The governing equations are developed from the energy functional V including von Kármán large-deflection expressions. The detailed derivation of the differential equations from the energy functional via the calculus of variations is found in Wadee and Hunt [2] for the case of an orthotropic core:

$$\begin{aligned} EIw'''' + D \left[2\Delta w'' + q_t \frac{b\pi^2}{L} \left(\sin \frac{\pi x}{L} w'' + \frac{\pi}{L} \cos \frac{\pi x}{L} w' \right) - (2u''w' + 2u'w'' + 3w'^2 w'') \right] \\ + G \left[\frac{u'}{b} - \frac{2}{3}w'' + (q_s - q_t) \frac{\pi^2}{L} \sin \frac{\pi x}{L} \right] + C_x \left[\frac{2}{3}\Delta w'' - \left(\frac{1}{2}u''w' + \frac{1}{2}u'w'' + \frac{3}{5}w'^2 w'' \right) \right. \\ + q_t \frac{b\pi^2}{6L} \left(\sin \frac{\pi x}{L} w'' + \frac{\pi}{L} \cos \frac{\pi x}{L} w' \right) \left. \right] + C_y \left[\frac{2}{3}\nu_x (w w'' + w'^2) - \nu_x \left(u' + \frac{1}{3}w'^2 \right) \right. \\ \left. - \frac{2}{3}\nu_x^2 \Delta b w'' \right] + kw - k_1 w^2 + k_2 w^3 = 0 \end{aligned} \quad (7)$$

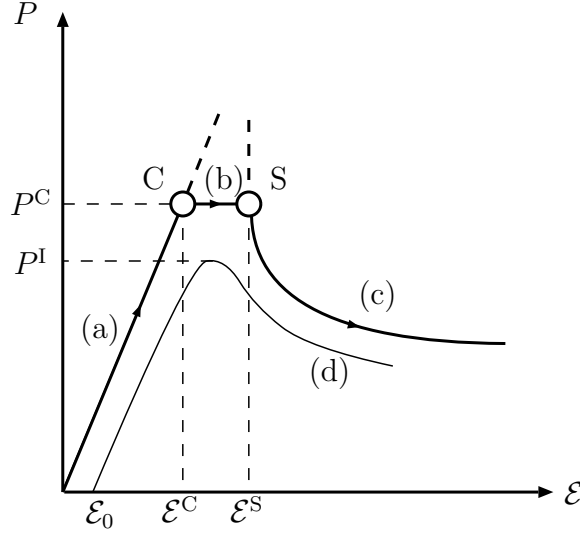


Figure 3: Equilibrium diagram for sandwich panels: (a) Fundamental path; (b) Critical path of overall buckling; (c) Secondary path of interactive buckling; (d) Typical imperfect path with limit load P^I . C: Critical bifurcation; S: Secondary bifurcation.

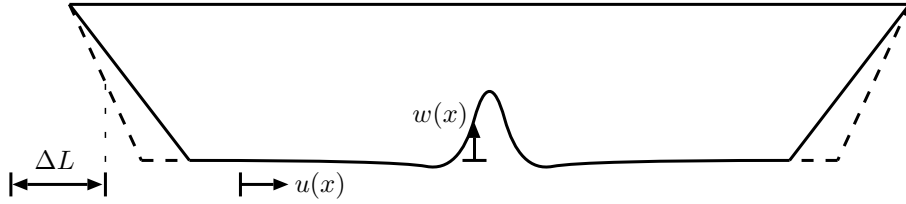


Figure 4: Displacement functions used to describe interactive buckling. Δ is the generalized coordinate for pure compression

$$\begin{aligned} & \left(D + \frac{C_x}{3}\right) u'' - \frac{G}{2b} \left(\frac{2}{b}u - w'\right) + \left(D + \frac{C_x}{4}\right) w'w'' - \frac{C_y\nu_x}{2}w' \\ & + \frac{G\pi}{b} \cos \frac{\pi x}{L} \left[(q_s - q_t) - \frac{q_t}{s}\right] = 0. \end{aligned} \quad (8)$$

Equations (7) and (8) respectively describe the lateral in-plane deflection of the face plate under greater compression. The differential equations are also subject to the following integral constraints, determined by minimizing V with respect to the generalized coordinates q_s , q_t and Δ [1]:

$$P = \frac{2\pi^2 EI}{L^2} + \frac{2G}{q_s} \left[(q_s - q_t) + \frac{1}{\pi L} \int_0^L \cos \frac{\pi x}{L} \left(w' - \frac{2}{b}u \right) dx \right], \quad (9)$$

$$s(q_s - q_t) = q_t + \int_0^L \left[\frac{s}{\pi L} \cos \frac{\pi x}{L} \left(\frac{2}{b}u - w' \right) - \frac{1}{b\pi^2} \sin \frac{\pi x}{L} \left(u' + \frac{1}{2}w'^2 \right) \right] dx, \quad (10)$$

$$\Delta = \frac{P + \int_0^L \left[\frac{2D}{L} \left(u' + \frac{1}{2}w'^2 \right) + \left(\frac{C_x - C_y\nu_x^2}{L} \right) \left(u' + \frac{1}{3}w'^2 \right) \right] dx}{4D + 2C_x - 2C_y\nu_x^2 b}. \quad (11)$$

where additional quantities are defined:

$$C_y = \frac{kb}{2}, \quad s = \frac{2GL^2}{b^2\pi^2} \left(D + \frac{C_x}{6} \right)^{-1}.$$

The panel is assumed to be simply-supported—Equation (12), and matching the applied stress at the ends give the in-plane boundary conditions—Equation (13):

$$w(0) = w''(0) = w(L) = w''(L) = 0, \quad (12)$$

$$-\frac{P}{4D} = \left(1 + \frac{C_x}{3D} \right) u'(x_0) + \left(1 + \frac{C_x}{4D} \right) \frac{1}{2} w'^2(x_0) - \left(1 + \frac{C_x}{2D} - \frac{C_y \nu_x^2 b}{2D} \right) \Delta. \quad (13)$$

3 Experimental Panels

A variety of different materials were used for the experimental panels, to obtain results that represented a fairly broad range. Pure aluminium or aluminium alloy were used for the face plates because of their more straightforward elastic responses; these materials had consistent material properties taken as, $E = 69 \text{ kN/mm}^2$ and $\nu = 0.3$, with their stress–strain relationships given in Fig. 5. The stress limits for linear elasticity (σ_{Lin}) for the pure aluminium and the aluminium alloy were 8 N/mm^2 and 95 N/mm^2 respectively. Various core materials were used and in these it was chosen to use noncellular foams, specifically polystyrene, polyurethane and rubber foams because of their reasonably homogeneous nature. Of these core materials, the polystyrene foam was the stiffest axially and in shear, followed by the polyurethane and the rubber foams respectively.

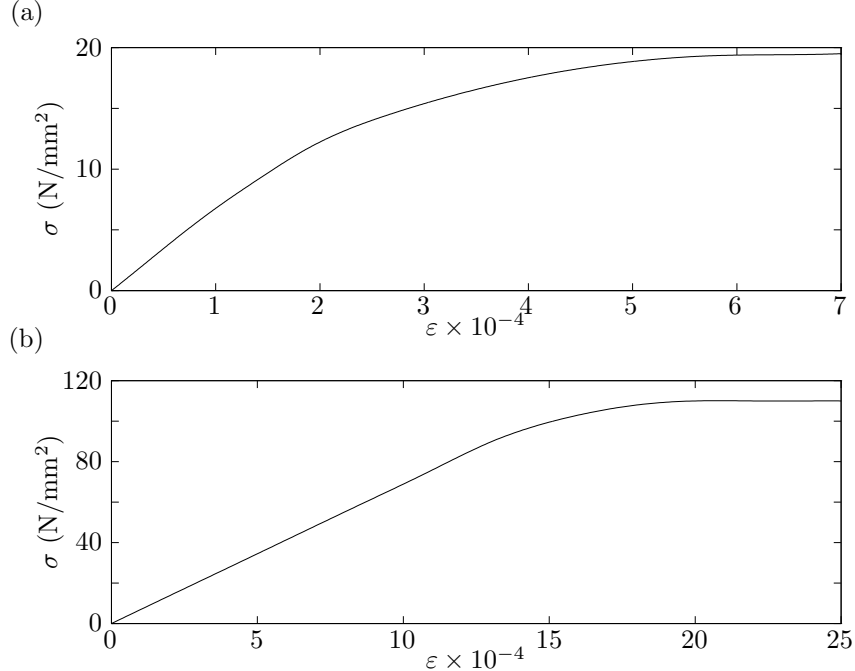


Figure 5: Stress–strain curves for (a) pure aluminium and (b) aluminium alloy. Linear elasticity is valid up to (a) $\sigma_{\text{Lin}} = 8 \text{ N/mm}^2$ for pure aluminium and (b) $\sigma_{\text{Lin}} = 95 \text{ N/mm}^2$ for aluminium alloy.

The bonding agent used to fix face plates to the core was altered also as the core changed; a flexible glue such as “Evo-stik” was preferable, and was used in conjunction

with the polyurethane and rubber foam cores. A degree of flexibility in the glue is desirable in the hardened state, as the action of buckling introduces small differential displacements at the face–core interface. If flexibility is not a property of the glue, problems of the core separating from the face become apparent, which is termed *delamination* in this paper. However, Evo-stik was found to dissolve polystyrene cores, and so a type of epoxy resin was used; this had the disadvantage (in most the tests) of not having the flexibility to cope with the deflection at the face–core interface without promoting delamination in its hardened state.

3.1 Apparatus

Two testing machines were used. Principally, the Instron 1 Tonne benchtop testing machine—Fig. 6(a) was employed for the majority of the testing of the panels and to determine individual material properties. A Denison 10 Tonne machine was also used on occasions, but gave fewer quantitative results—Fig. 6(b). The Instron machine had the advantages that the rate of loading could be accurately controlled electronically and gave output of load–displacement automatically; the Denison machine was controlled via a less accurate manual hydraulic valve, and load–displacement plots were not possible without resorting to strain gauging the test panel accurately—which would have significantly increased the expense of this series of experiments.



(a) Instron 1 tonne benchtop testing machine.



(b) Denison 10 tonne testing machine.

Figure 6: Experimental testing machines.

3.2 Panel Construction and Core Testing

All panels were constructed with a very straightforward method, similar to the *wet lay-up* method described by Karlsson and Åström [12]. Face plates were first coated with the glue, and then once the glue began to harden, the core and the faces were bonded together

with pressure applied laterally to hold the wet panel in place. Once the glue had set, the testing commenced. The loading configuration as represented schematically in Fig. 1 was in reality as shown in Fig. 7(a), with (b) and (c) showing the sequential response of the panel under axial compression. For the comparisons between theory and experiment, the cores for the theoretical model are assumed to be orthotropic owing to the non-isotropic relationship of axial and shear moduli. However, to keep the model simple, it is assumed that $E_c = E_x = E_y$ and $\nu_c = \nu_x = \nu_y$.

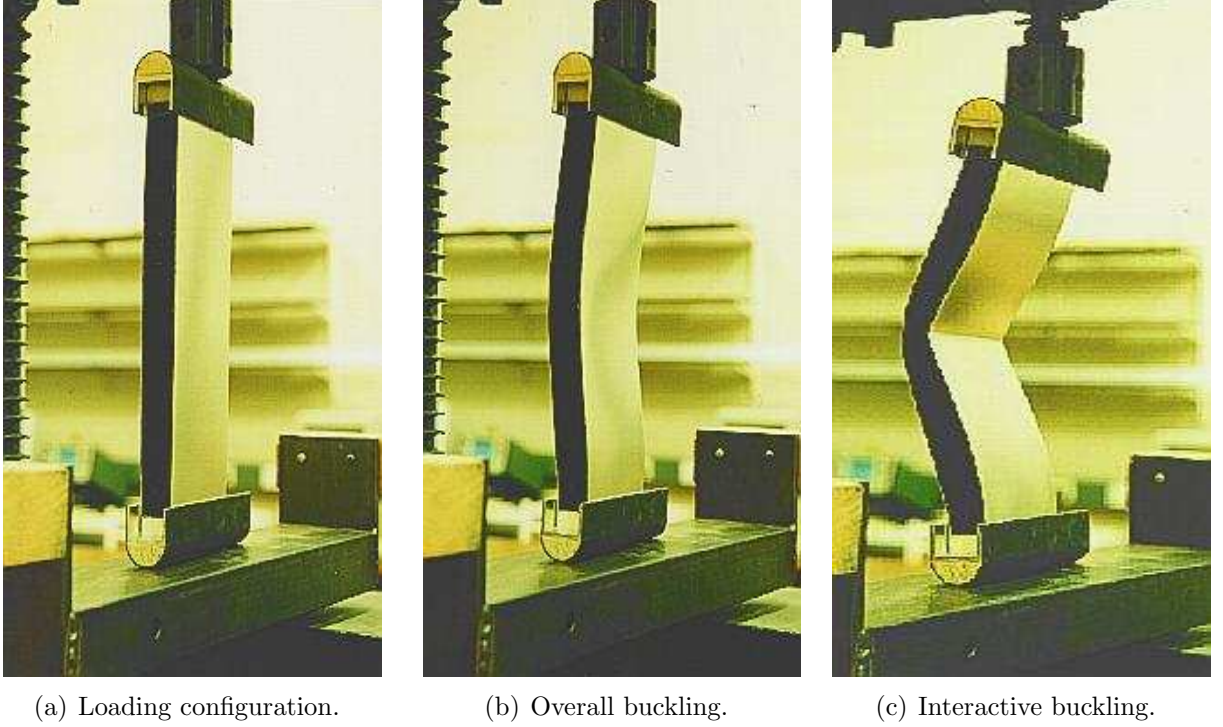


Figure 7: Response under loading.

Core materials were tested for their axial and shear stiffness. Simple cube compression tests (Fig. 8) gave axial moduli and Poisson's ratios; a slightly more complicated test for measuring the shear modulus was derived from a similar test devised by Demsetz and Gibson [13], with its configuration schematically represented in Fig. 9.

For the core axial modulus, the cube samples were compressed by a force F_c , as shown in Fig. 8, under displacement δ giving load-displacement graphs. The axial modulus E_c is, as usual, given by the initial linear portion of the stress-strain response. Thus,

$$E_c = \frac{\text{direct stress}}{\text{direct strain}} = \frac{F_c/(b_1 b_2)}{\delta/b_3} = \frac{F_c b_3}{b_1 b_2 \delta}. \quad (14)$$

The Poisson's ratio was estimated by the small amount of *barrelling* or transverse dilation exhibited by the cube sample. The initial width was compared to the widths under loading at three locations along the depth of the cube; from this, ε_y was obtained and so ν_c was estimated

$$\varepsilon_y = \text{Maximum of } \frac{b_{1\text{final}} - b_{1\text{initial}}}{b_{1\text{initial}}},$$

$$\nu_c = \frac{\varepsilon_y}{\delta/b_3}. \quad (15)$$

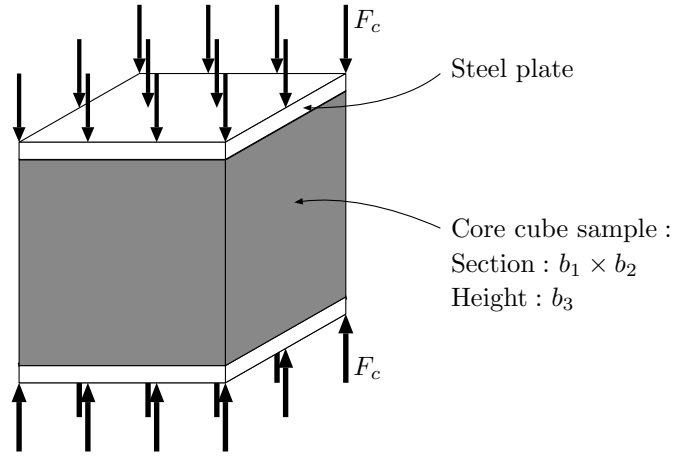


Figure 8: Test for measuring axial modulus E_c of cores.

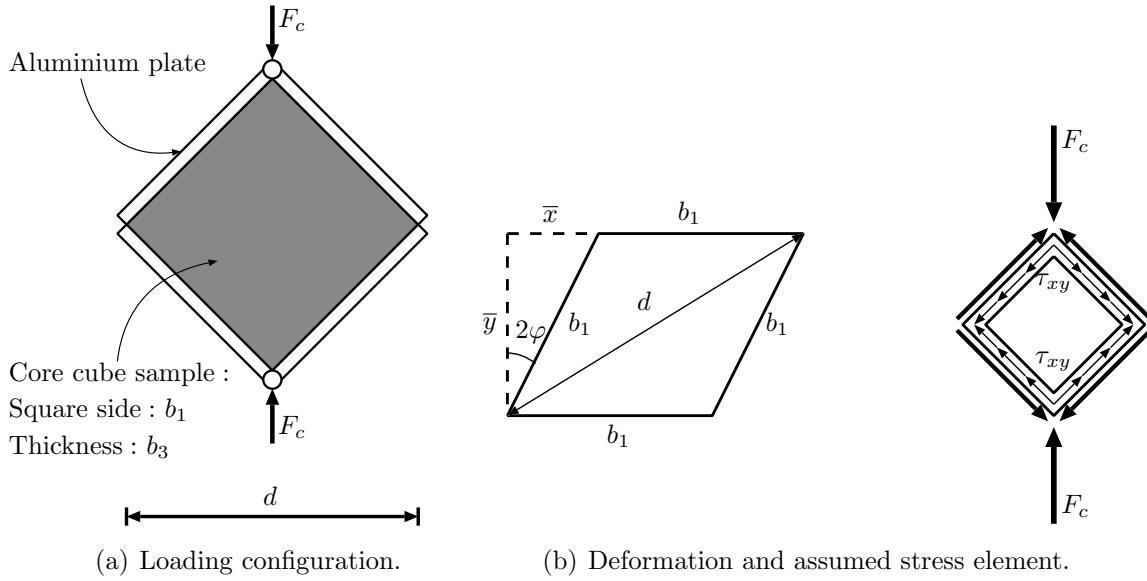


Figure 9: Test for measuring shear modulus G_c of cores.

The shearing test is slightly more complicated: if the force F_c causes the square sample of side b_1 and thickness b_3 , to splay by an angle 2φ (that is by φ each side of the axis of loading), then this is equal to the shear strain γ_{xy} . By measuring the diagonal distance, d , the expression for the shear strain is derived from the following geometric analysis of Fig. 9(b):

$$\bar{x} = b_1 \sin 2\varphi, \quad \bar{y} = b_1 \cos 2\varphi.$$

By Pythagoras' theorem we obtain

$$(b_1 + \bar{x})^2 + \bar{y}^2 = d^2,$$

which gives

$$2\varphi = \arcsin \left(\frac{d^2}{2b_1^2} - 1 \right) = \gamma_{xy}.$$

Considering a small element under the oblique loading F and resolving forces while assum-

ing the shear stress τ_{xy} is uniform along the edges gives an expression after manipulation:

$$\tau_{xy} = \frac{\sqrt{2}}{2} \left(\frac{F_c}{b_1 b_3} \right).$$

From this, the shear modulus is

$$G_c = \frac{\text{shear stress}}{\text{shear strain}} = \frac{\tau_{xy}}{\gamma_{xy}} = \frac{\sqrt{2}}{4} \left(\frac{F_c}{b_1 b_3 \varphi} \right). \quad (16)$$

Two specimens were tested for each material, all of dimensions: $b_1 = 75$ mm and $b_3 = 24$ mm. From the axial and shear modulus tests, the average values of the moduli were as given in Table 1.

Core material	E_c	G_c	ν_c	k_1	k_2
Polystyrene foam	8.8	4.2	0.05	80.2	18.7
Stiff Polyurethane foam	5.0	2.5	0.05	82.3	32.0
Soft Polyurethane foam	0.2	0.10	0.05	0.22	0.007
Rubber foam	0.4	0.25	0.10	0.11	0

Table 1: Experimental values of elastic moduli E_c and G_c in N/mm² and Poisson’s ratio ν_c for core materials with nonlinear constitutive law constants k_1 (N/mm³) and k_2 (N/mm⁴).

4 Test Panel Results

4.1 Failure Modes

There were various different modes of failure exhibited during the series of tests. Other than the localized buckling of interest here and which is discussed later, failure owing to face–core delamination—Fig. 10(a)—occurred quite often as in experimental study of Lingaiah and Suryanarayana [14], particularly with the polystyrene cores in conjunction with epoxy resin glue, as did failure owing to core fracture in shear after overall buckling—Fig. 10(b).

The face–core delamination, when it occurred, was always triggered immediately after overall buckling. The shearing in the core after overall buckling, modelled theoretically by the sway and the tilt modes, requires the interface of the face and core to move in sympathy with the rest of the core. If face–core movement is virtually constrained by the glue, because of its intrinsic rigidity in its hardened state, the face plate finds it easier to move outwards and so delamination occurs. The core fracturing is explained simply by the core having insufficient strength to cope with the shear stresses involved in the overall buckling; only the panels with stiff polyurethane cores exhibited this mode and so the panel geometry was changed to reduce the shear stresses and eliminate core fracture.

Consider now the failure mode of particular interest—overall buckling followed by an interactively induced localized buckle on one face. Figs. 7(a)–(c) show a typical sequence which theoretically in the perfect case would yield results resembling paths (a)–(c) respectively, from Fig. 3. However, owing to unavoidable initial imperfections, the response resembles path (d) from Fig. 3; Fig. 7(a) represents a point on the positive gradient path, the form of Fig. 7(b) occurs at the maximum point where $P = P^I$ and deflections of the

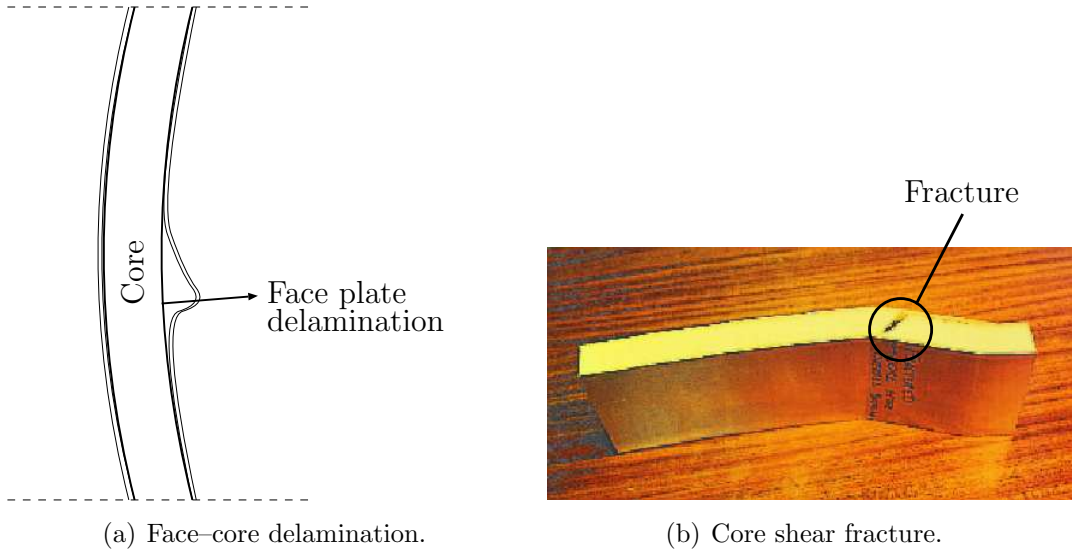


Figure 10: Failure modes other than localized buckling.

form of Fig. 7(c) occur on the negative gradient path, where the panel loses strength and eventually enters into the plastic range.

To compare the interactive buckling model with the experiments, the general buckle pattern and its localized wavelength (defined below) can be considered. The experimental buckle pattern is determined by measuring the maximum amplitude of the localized buckle, the locations along the length of the first minima either side of the maximum, and the distance between the minima—defined as the localized buckle wavelength λ , as shown in Fig. 11. These minima in the buckle profile were relatively difficult to discern with the naked eye and so electronic vernier calipers were used to measure the respective minima while the panel was in the loaded state; the precision of this was within 0.1 mm. For determining the location of the minima, a standard ruler was used and this was only precise to the nearest millimetre. For numerical comparisons, the geometric and material properties of the experimental panels are substituted along with suitable approximations for the nonlinear core constitutive laws [15]; cubic for the polystyrene and polyurethane cores with progressive stiffnesses that go from positive to approximately zero to positive, and a small quadratic nonlinearity for the rubber foam core. The difference in the nonlinearity reflects the difference in the response of the rubber foam core in compression compared to the others.

The numerical continuation package *AUTO* [16] is used to solve the system of differential equations—Equations (7)–(8)—subject to the integral constraints in Equations (9)–(11) and the boundary conditions—Equations (12)–(13)—of the interactive buckling model [1, 2]. Comparisons of buckle profile are made by first matching the maximum buckle amplitude by controlling end-displacement, then the difference in the experimental wavelength λ_{Expt} and the theoretical wavelength λ_{Th} is determined. For all cases except the polystyrene core panels, the (imperfect) experimental and (perfect) theoretical load–end-shortening curves are also compared.

In most of the tests, it is found that the experimental wavelength correlate very well with the theory; experimental load–end-shortening curves are also well inside the theory because bifurcation corners are rounded off by initial geometric imperfections [3].

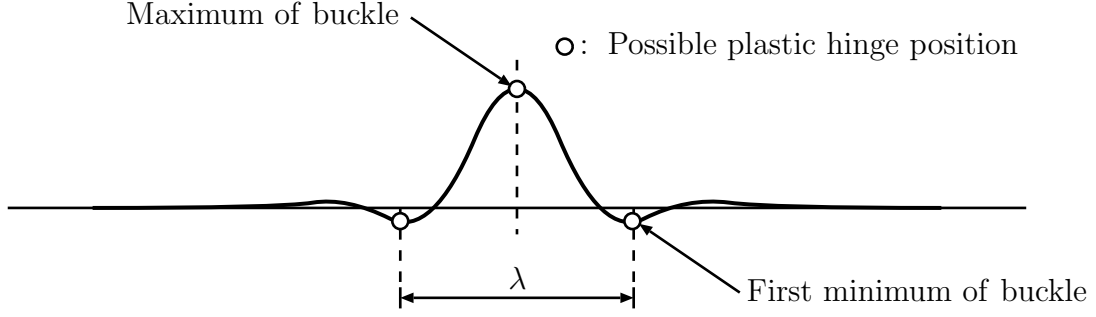


Figure 11: Definition of localized buckle wavelength.

4.2 Results Compared with Theory

Table 2 lists the successful experimental panels and describes their core materials and geometry, together with the testing machine used and the experimental effective length (L_e) which was physically measured during the experiment. The variation of the effective

Panel	Face	Core	Machine	c	b	t	L	L_e
1	Alloy	Ps	Denison	70	25	0.25	292	322
2	Alloy	Ps	Denison	152	25	0.25	292	322
3	Alloy	StPu	Instron	90	25	0.9	470	500
4	Alloy	SoPu	Instron	100	25	1.0	300	210
5	Alloy	SoPu	Instron	100	25	1.0	300	210
6	Alloy	SoPu	Instron	100	25	1.0	300	210
7	Pure	Ru	Instron	102	25	1.0	300	210
8	Pure	Ru	Instron	102	25	1.0	300	210
9	Pure	Ru	Instron	102	25	1.0	300	210
10	Pure	Ru	Instron	102	25	1.0	300	210

Table 2: Test panel geometries where face and cores are denoted. Face materials—Alloy: Aluminium Alloy; Pure: Pure Aluminium. Core materials—Ps: Polystyrene foam; StPu: Stiff Polyurethane foam; SoPu: Soft Polyurethane foam; Ru: Rubber Foam. All dimensions are in millimetres.

lengths reflect the difference in the end-plates used in the tests. For panels 1–3, the end-plates were as shown in the photograph in Fig. 12. These larger end-plates were made from steel, and seemed to give an effective pin at the end of the panel. For the remainder of the tests, the end-plates were those as shown in Fig. 7. These smaller end-plates were constructed from wood and had a rubber surface. This increased the friction at the ends and reduced the panel L_e value, and was the only significant difference in the experimental response owing to the difference of the supports.

Table 3 shows the theoretical critical load P^C and compares them with the experimental collapse load P^I . It also shows whether the axial stress σ_x , where

$$\sigma_x = P^I/(2ct),$$

at the point of buckling during the experiment, exceeds the linear elastic stress limit (σ_{Lin}) for the face plate; it turns out that none of the tested panels exceed linear elastic stresses

before buckling. In the cases for panels 1–3, the modal buckling loads P_l^C and P_o^C are seen

Panel	c	P_o^C (kN)	P_l^C (kN)	P_l^C/P_o^C	P^I (kN)	P^I/P^C	σ_x/σ_{Lin}
1	70	6.07	6.67	1.100	2.90	0.48	0.872
2	152	13.17	14.49	1.100	5.65	0.43	0.783
3	90	5.23	14.91	2.848	3.69	0.71	0.240
4	100	0.543	3.223	5.932	0.560	1.031	0.029
5	100	0.543	3.223	5.932	0.605	1.114	0.032
6	100	0.543	3.223	5.932	0.590	1.087	0.031
7	102	0.925	4.658	5.035	1.010	1.092	0.619
8	102	0.925	4.658	5.035	0.872	0.943	0.534
9	102	0.925	4.658	5.035	0.920	0.995	0.564
10	102	0.925	4.658	5.035	0.950	1.027	0.582

Table 3: Theoretical (P^C) and Experimental (P^I) buckling loads for all test panels. Ratio of axial stress (σ_x) to limiting face plate linear elastic stress (σ_{Lin}).

to be relatively closer together than for the remainder of the panels. This suggests that the post-buckling responses for the panels with buckling loads closer together are likely to be more severe than the remainder. This is borne out by the experimental results, which show that panels 1–3 do not come near to reaching P^C , whereas the remaining panels 4–10, either reach or nearly reach their P^C . Another noteworthy point is that although panels 4–10 reach their P^C and theoretically have critical and secondary bifurcations which are far apart, they also rapidly exhibit negative post-buckling stiffness as soon as they reach P^C . Classically, structures with critical and secondary bifurcations far apart would remain at P^C for some time before deflections became large enough to induce yielding. It seems reasonable, however, that local changes in cross-section after overall buckling combined with plasticity effects, may have an important part in reducing the actual post-buckling stiffness—this point needs further investigation.

Theoretical post-buckling responses are shown in Figs. 13–16, where (a) show comparisons of buckle patterns, with the numerical comparison of localized buckle wavelength shown in Table 4, (b) show the load–end-shortening responses, and (c) show the nonlinear core constitutive relationship F used in the numerical calculations, where

$$F = F(w) = kw - k_1w^2 + k_2w^3.$$

These nonlinear models are designed to simulate the early linear elastic response followed by the nonlinear (quadratic) softening and subsequent restiffening. As *AUTO* found it difficult to converge with more accurate values for the cubic stiffening for the stiffer cores (polystyrene and stiff polyurethane), k_2 was chosen in order to induce the restiffening after w/b had reached as high a value as possible without significantly affecting the (approximately) zero stiffness from the combination of the quadratic and cubic terms; a solution would have been to fit higher order polynomials to the experimental curves—increasing the complexity of the differential equations. However, numerical experiments showed the interactive buckling mode was governed by the initial linear portion and the first drop in stiffness to zero. Therefore, matching the linear portion and the initial drop in stiffness accurately were of paramount importance, whereas the importance of accurately modelling

the subsequent restabilization only increased further into the post-buckling régime. Note also that the sequential snap-back spikes of restabilization appear in the theoretical response of the stiff polyurethane core panel—Fig. 14(b)—[17], but are incidental to the salient response.

Closeup photographs of selected panels with their theoretical localized buckle wavelengths are shown in Fig. 17. The results for the buckle pattern wavelength suggest good correlation with the nonlinear model—both short and long wavelength localized buckling seem to compare favourably with the experimental results. However, for the softer cores—the soft polyurethane and rubber foam—the troughs of the theoretical buckle pattern do not match well. It is conjectured that large strains introduce plastic hinges in the face plates at locations highlighted in Fig. 11. Nevertheless, as the buckle wavelengths correlate well, plasticity would only be an addition to an already well-developed theoretical model.

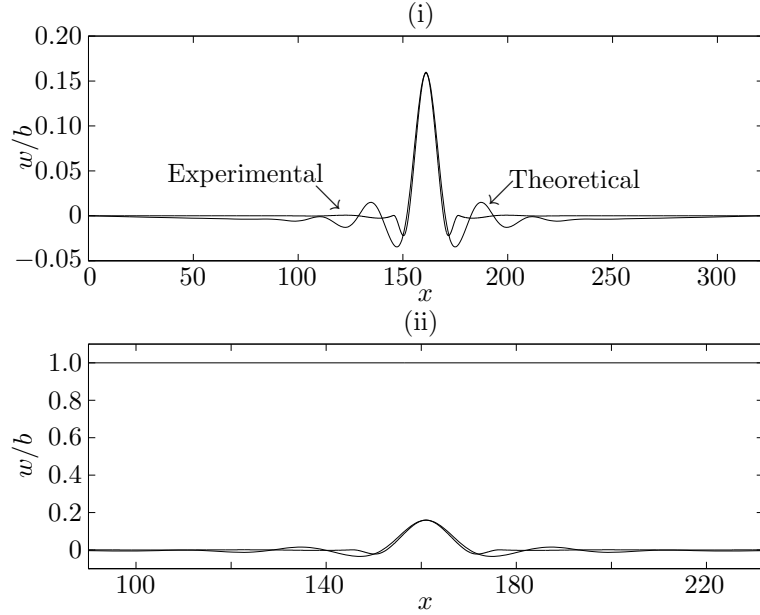
Comparisons of load–end-shortening graphs show that for the stiffer cores, where the theoretical critical and secondary bifurcations are much closer together than for the softer cores, the experimental collapse load is well below the theoretical critical load—implying a high degree of imperfection sensitivity [3]. For the softer cores, however, the load reaches the critical load but almost immediately, with the onset of localization, the structural stiffness effectively becomes negative implying a progressive reduction in panel strength.

Panels	Core	$(\lambda_{\text{Th}} - \lambda_{\text{Expt}}) / \lambda_{\text{Th}}$
1–2	Ps	0.154
3	StPu	0.378
4–6	SoPu	0.029
7–10	Ru	0.016

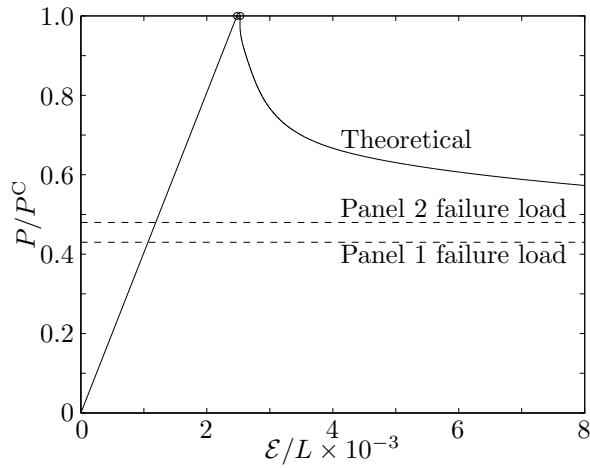
Table 4: Comparison of theoretical and experimental localized buckle wavelengths λ .



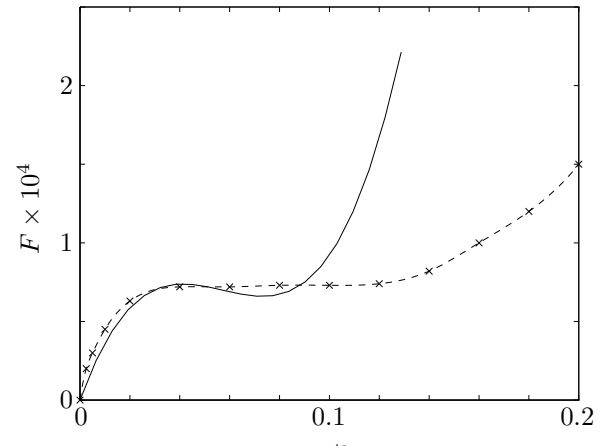
Figure 12: Polystyrene core panel in Denison testing machine: note the end supports.



(a) Comparison of buckle pattern at $P/P^C = 0.55$. (i) Comparison showing full panel length. (ii) Same as (i) but w/b axis expanded to show other face plate ($w/b = 1$).

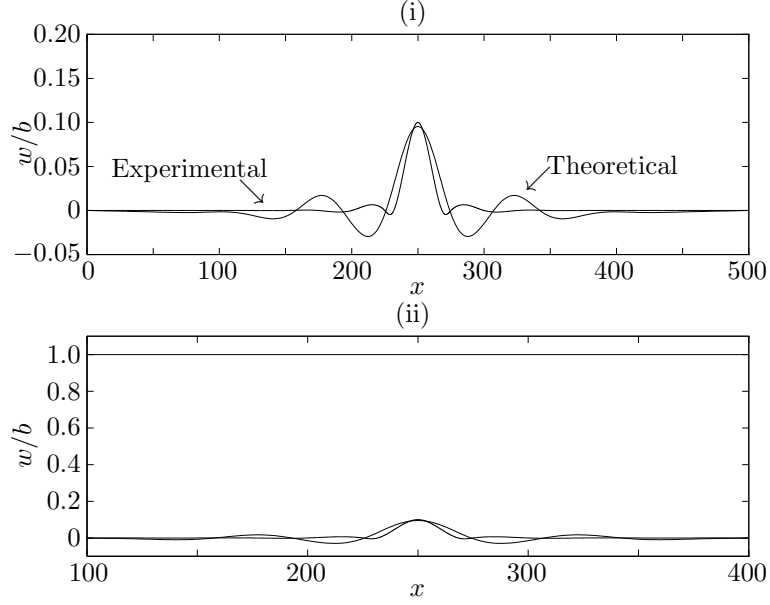


(b) Load-end-shortening curve comparison.

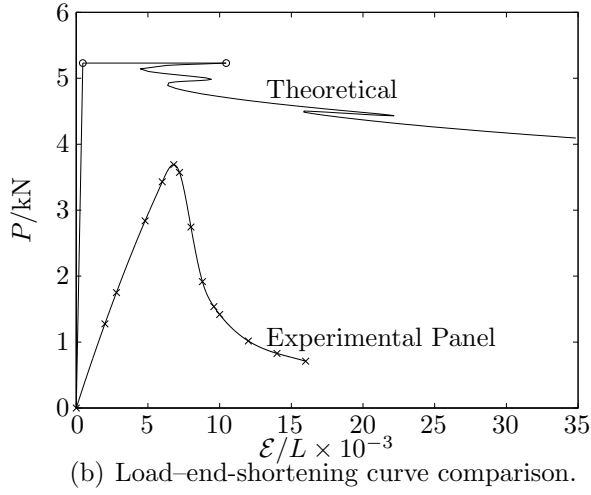


(c) Nonlinear constitutive relationship for core. Dashed line shows average experimental response.

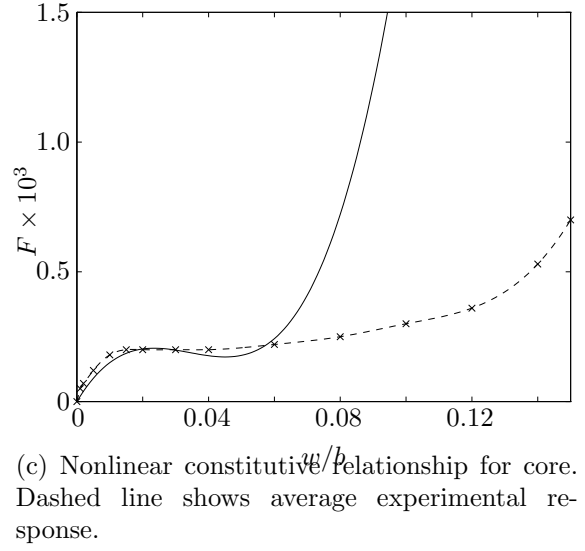
Figure 13: Interactive model against experiments for polystyrene core panels.



(a) Comparison of buckle pattern at $P/P^C = 0.95$. (i) Comparison showing full panel length. (ii) Same as (i) but w/b axis expanded to show other face plate ($w/b = 1$).

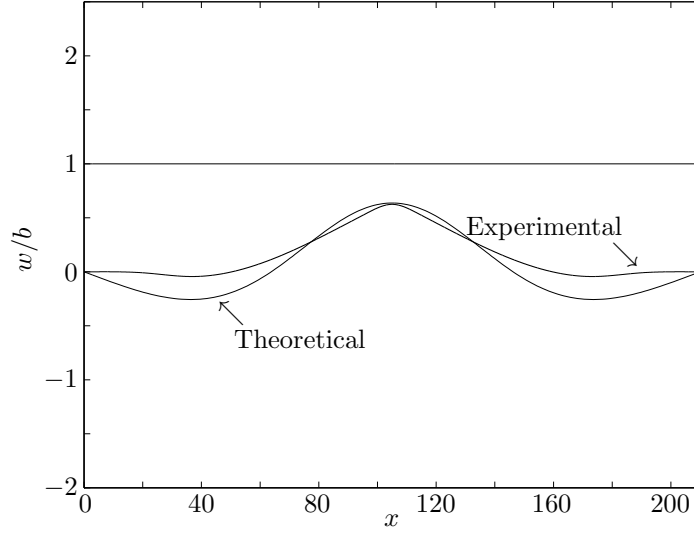


(b) Load-end-shortening curve comparison.

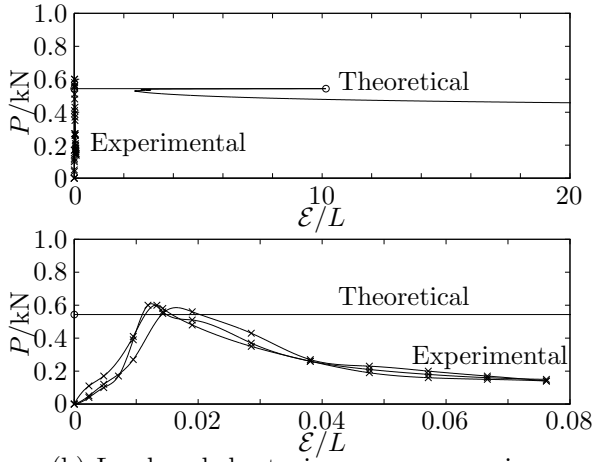


(c) Nonlinear constitutive relationship for core. Dashed line shows average experimental response.

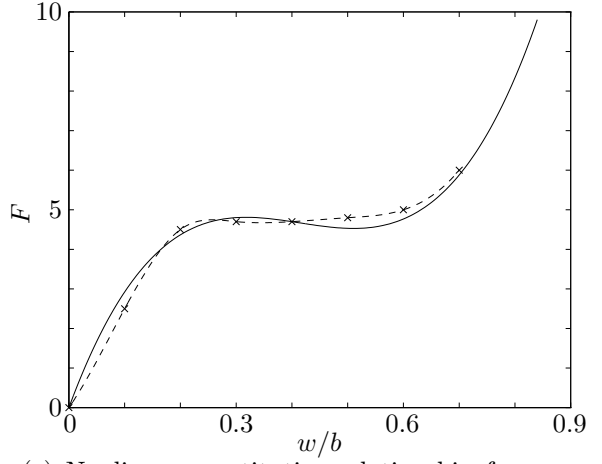
Figure 14: Interactive model against experiment for stiff polyurethane foam core panel.



(a) Comparison of buckle pattern at $P/P^C = 0.975$.

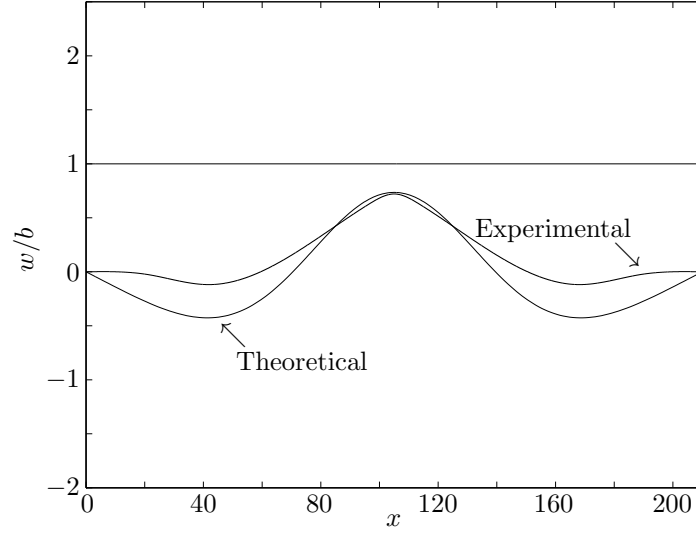


(b) Load-end-shortening curve comparison.

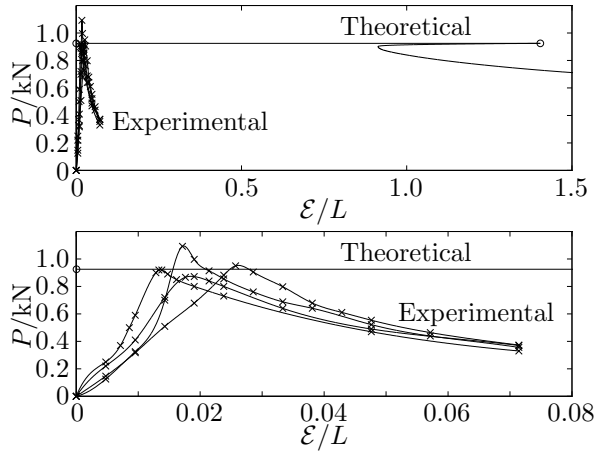


(c) Nonlinear constitutive relationship for core. Dashed line shows average experimental response.

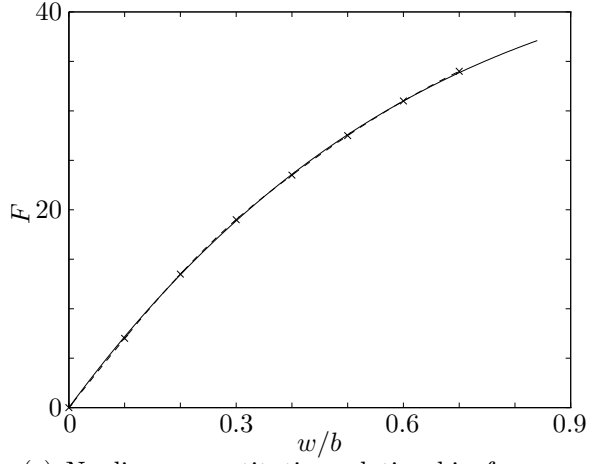
Figure 15: Interactive model against experiments for soft polyurethane foam core panels.



(a) Comparison of buckle pattern at $P/P^C = 0.87$.



(b) Load-end-shortening curve comparison.



(c) Nonlinear constitutive relationship for core. Dashed line shows average experimental response.

Figure 16: Interactive model against experiments for rubber foam core panels.

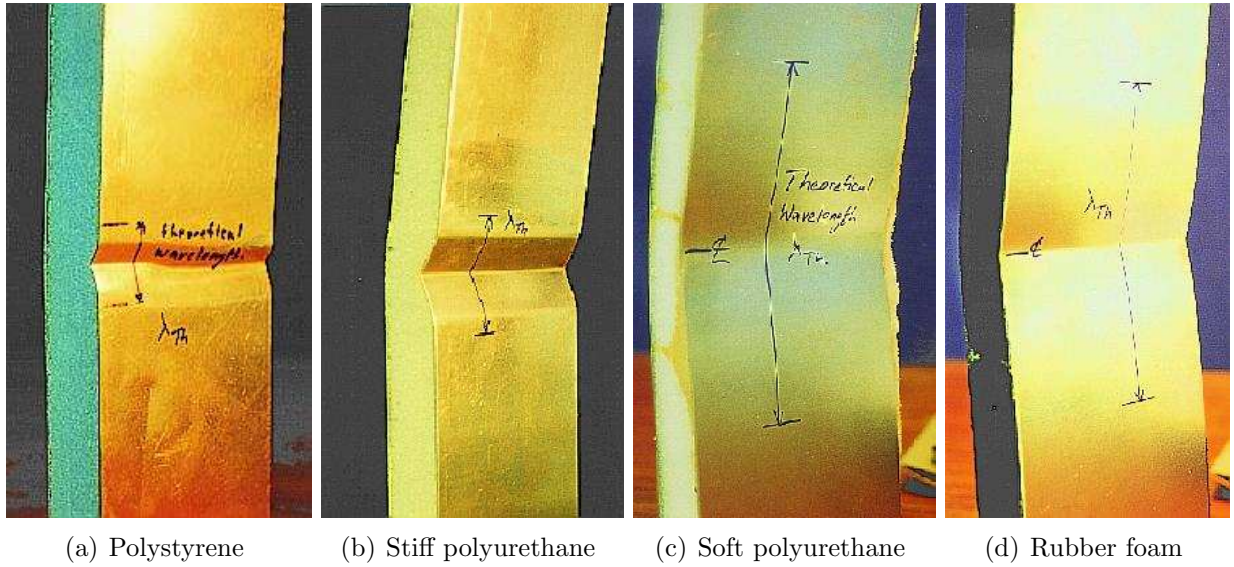


Figure 17: Photographs of buckle pattern with theoretical localized buckle wavelength marked on tested panels.

5 Concluding Remarks

This paper has presented quite a varied series of simple physical experiments of axially-loaded sandwich panels and compared them with the interactive buckling model developed earlier. The results are quite noteworthy because a range of core materials were tested and that experimental failure loads compared well with critical loads, experimental localized buckle wavelengths compared very favourably with theory, and load–displacement graphs were also acceptable.

The comparison with theory and experiment is quantitatively good for the localized buckle wavelengths—short wavelengths for stiffer cores were predicted as were long wavelengths for softer cores. The experiments show good agreement with the theory. The comparison of failure loads and linear critical loads have been qualitatively good because it implies that when linear buckling loads of separate modes are near coincidence, the failure load is well below these linear critical loads. The reverse has been shown as well, where separate modes are far apart, panels at least reach their linear critical loads, even though they tend to exhibit negative stiffness soon after buckling. To obtain better quantitative results for the failure loads, where the critical modes nearly coincide, it would be necessary to conduct more complex tests where imperfections are carefully measured in the panels in the generic style of, amongst others, Roorda [18]. This could be then compared with the sandwich panel model incorporating initial geometric imperfections, introduced by Wadee [3] which would give a quantitative value of the failure load, P^I . The same type of approach would be necessary for the full post-buckling characteristics, even though the present interactive buckling model seems to give strong indications when and when not to expect the panel to fail at its linear critical load.

However, with experimental panels failing well below their critical loads and interactive localized buckling inducing negative post-buckling stiffnesses, near-coincident critical loads combined with initial imperfections are indeed important ingredients for highly unstable responses to be exhibited by compression sandwich panels.

Acknowledgement

Financial support for the author was provided by a University of Bath Studentship.

References

- [1] G. W. Hunt and M. Ahmer Wadee. Localization and mode interaction in sandwich structures. *Proc. R. Soc. Lond., A* 454(1972):1197–1216, 1998.
- [2] M. Ahmer Wadee and G. W. Hunt. Interactively induced localized buckling in sandwich structures with core orthotropy. *Trans. ASME J. Appl. Mech.*, 65(2):523–528, 1998.
- [3] M. Ahmer Wadee. Effects of periodic and localized imperfections on struts on non-linear foundations and compression sandwich panels. *Int. J. Solids Struct.*, 1999. In press.
- [4] S. Kodiyalam, S. Nagendra, and J. DeStefano. Composite sandwich structure optimization with application to satellite components. *AIAA J.*, 34(3):614–621, 1996.
- [5] J. M. T. Thompson and G. W. Hunt. *A general theory of elastic stability*. Wiley, London, 1973.
- [6] B. Budiansky, editor. *Buckling of Structures*. IUTAM Symposium, Cambridge, USA, 1974. Springer, Berlin, 1976.
- [7] W. T. Koiter and M. Pignataro. A general theory for the interaction between local and overall buckling of stiffened panels. Technical Report WTHD 83, Delft University of Technology, Delft, The Netherlands, 1976.
- [8] G. W. Hunt, L. S. Da Silva, and G. M. E. Manzocchi. Interactive buckling in sandwich structures. *Proc. R. Soc. Lond., A* 417(1852):155–177, 1988.
- [9] H. G. Allen. *Analysis and design of structural sandwich panels*. Pergamon, Oxford, 1969.
- [10] L. A. P. Simões Da Silva. *Modal interactions in bending and buckling of sandwich structures*. PhD thesis, Imperial College of Science, Technology and Medicine, London, 1989.
- [11] M. Ahmer Wadee. *Localized buckling in sandwich structures*. PhD thesis, University of Bath, 1998.
- [12] K. F. Karlsson and B. T. Åström. Manufacturing and applications of structural sandwich components. *Composites Part A*, 28A(2):97–111, 1997.
- [13] L. A. Demsetz and L. J. Gibson. Minimum weight design stiffness in sandwich plates with rigid foam cores. *Mat. Sci. Eng.*, 85(1–2):33–42, 1987.
- [14] L. Lingaiah and B. G. Suryanarayana. Strength and stiffness of sandwich beams in bending. *Expt. Mech.*, 31(1):1–7, 1991.

- [15] L. J. Gibson and M. F. Ashby. The mechanics of three-dimensional cellular materials. *Proc. R. Soc. Lond.*, A 382(1782):43–59, 1982.
- [16] E. J. Doedel, X-J. Wang, and T. F. Fairgrieve. AUTO94: Software for continuation and bifurcation problems in ordinary differential equations. Technical Report CRPC-95-2, California Institute of Technology, 1995.
- [17] G. W. Hunt, M. A. Peletier, A. R. Champneys, P. D. Woods, M. Ahmer Wadee, C. J. Budd, and G. J. Lord. Cellular buckling in long structures. *Nonlinear Dynamics*, 1998. Special issue on Localization. To appear.
- [18] J. Roorda. The buckling behaviour of imperfect structural systems. *J. Mech. Phys. Solids*, 13:267–280, 1965.